JOURNAL OF MATERIALS SCIENCE **38** (2003) 4765–4776

The influence of silica fume on the corrosion resistance of steel in high performance concrete exposed to simulated sea water

T. D. MARCOTTE
CVM Engineers, 85 Old Eagle School Road, Wayne, PA 19087, USA
E-mail: tdm@cvmengineers.com

C. M. HANSSON
Department of Mechanical Engineering, University of Waterloo, Waterloo, Ontario N2L 3G1, Canada

This investigation examined the influence of silica fume on the corrosion behaviour of steel in high performance concrete (HPC) by comparing the behaviour of HPC concretes with and without a 10% by mass of cement addition of silica fume. Reinforced concrete prisms (500 × 100 × 100 mm) with embedded corrosion probes were loaded in three-point bending to achieve a 0.3 mm crack and exposed to simulated sea water for up to four years. Corresponding prisms without induced cracks were also studied as controls. For the HPC with silica fume, pore size distribution measurements showed that after exposure to the simulated sea water, the hydration and pozzolanic reactions near the induced crack blocked almost all continuous pores in the 0.01 to 10 μm range. This affected the type and distribution of corrosion products that formed by restricting the access of chlorides and oxygen to the surface of the steel. Thus, only magnetite (Fe_3O_4) formed and was confined the space provided by the induced crack, effectively plugging the crack. In HPC without silica fume, oxygenated corrosion products such as goethite (α-FeOOH) and akaganeite (β-FeOOH) formed in the induced crack region. The implications of these observations on the service life of high performance concrete structures are discussed. © *2003 Kluwer Academic Publishers*

1. Introduction

Canada's infrastructure has been estimated to have a yearly cost of $3 billion to taxpayers but surveys of Canadian municipalities have indicated a financial shortfall in the rehabilitation of their infrastructure on the order of $20 billion [1]. Canada's situation is not unique, however, as the corrosion of steel reinforcement due to chloride exposure is a world-wide issue costing an inestimable amount for infrastructure repair and replacement. While the development of high performance concrete (HPC) was initially aimed at providing significantly higher strengths, its secondary goal has been to provide greater durability, including resistance to deleterious ions such as chlorides, and reduce future repair costs. The hypothesis has been that by reducing the water/cementitious materials ratio (w/cm) and providing adequate workability, compaction, and curing by the addition of appropriate chemical admixtures and procedures, the interconnected capillary porosity is greatly reduced, thereby limiting the ingress of chlorides or CO_2. It is for this reason that silica fume is considered essential to HPC mixes as it has been shown to virtually eliminate capillary porosity [2]. This low porosity should (i) reduce the diffusion of chlorides from the environment, thereby, delaying corrosion initiation and (ii) increase the electrical resistivity of the HPC and limit the subsequent corrosion rate. Under these circumstances, it anticipated that only cracked concrete would allow the ingress of sufficient chlorides to initiate and sustain the corrosion of the reinforcing steel. However, when the cracking behaviour of HPC has been investigated, it has been shown to have increased tensile strength corresponding to its increased compressive strength, but also increased brittleness [3, 4]. This brittleness has been attributed to its reduced capability to prevent crack propagation relative to conventional concretes [4]. As such, HPC may only be able to accommodate a relatively smaller volume of corrosion products before cracks are initiated.

Another approach to resolving escalating repair and rehabilitation costs has been the development of structural service life estimates to help prioritize the various repair programmes within the available financial resources. The success of these estimates has been limited, however: structural service life estimates are typically based upon empirical information collected from existing structures that were likely built using different concrete mix designs and situated within dissimilar environments. The recognition of this inaccuracy has increased attention towards developing theoretical models of corrosion that can be appropriately tailored for different materials and environments. Current service life models represent corrosion as a two-stage phenomenon: the time period prior to the initiation of corrosion, and the period thereafter while the damage accumulates to failure. Until recently it has been assumed that once corrosion initiates, the structural service life is over because the damage accumulation phase is comparatively smaller, and therefore, insignificant. This is now acknowledged not to be the case but modeling the damage accumulation phase is complex because of a lack of important information concerning the variation in corrosion rates during that period, and the corrosion products that form. Indeed, almost all research to date has focused on the time required for a sufficient number of chlorides to penetrate the concrete cover and initiate corrosion of the reinforcing steel (e.g., Delagrave *et al.* and Liang *et al.* [5, 6]). This need for further information was identified in a review paper by Pettersson and Sandberg who summarized factors affecting the chloride threshold level, the corresponding corrosion rates, and the influence of cracks in high performance concretes [7]. More recently, the effect of cracks on chloride transport properties in conventional concrete laboratory specimens [8] and field structures [9, 10] has been reported.

Thus, the goals of this investigation were to identify the corrosion products that form, determine where they form, and relate these observations to the microstructural characteristics of two high performance concretes, one with and one without silica fume, designated HPC/10%SF and HPC/0SF, respectively. To estimate the performance of these concretes in the field, the prisms studied in this investigation were analyzed in the cracked and statically loaded condition. It was the intent of this research programme to correlate corrosion rates with the volume of resulting corrosion products that can be accumulated before the concrete is damaged to provide insight into the consequential impact on the remaining lifetime of the structure and assist in the development of more accurate service life predictions.

2. Experimental programme

2.1. Prism preparation with five element corrosion probe

An embeddable corrosion probe system was developed as part of a larger Concrete Canada project [1] that facilitated a range of corrosion measurement techniques for laboratory and field research programmes: open circuit potential measurements, linear polarization resistance, electrochemical noise, and zero resistance ammetry. The system consisted of five pieces of rebar, each approximately 15 mm diameter and 30 mm long, which were attached to conventional reinforcing steel bar that acted as a "backbone." Each rebar element was at least 20 mm from neighboring elements, and electrically isolated from the aforementioned "backbone". Every rebar element also retained its original millscale and characteristic ribs. An electrical lead was soldered to one end of each element and the area of connection was coated with medium viscosity epoxy to protect it.

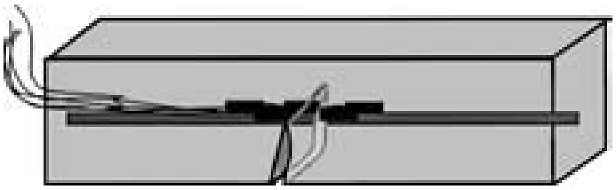

Figure 1 Detailed drawing of the concrete prisms with their embedded steel corrosion probe.

Four concrete prisms (500 × 100 × 100 mm) of both concrete types under investigation were mixed and cast with an embedded five element corrosion probe, detailed in Fig. 1, and the mixture proportions of the two concrete mixtures are given in Table I. The batching, mixing, and casting methods were typical of those practiced by the supplying ready-mix plant and placing contractor as it was the intent of this work to study concrete samples that were representative of the current Canadian construction standards at that time. Continuing within this concept, the prisms were covered with plastic sheets and field "cured" for two weeks. They were then stored outdoors for approximately three months. The physical properties of the concrete at 28 days are detailed in Table II.

TABLE I Mixture proportions of the cast concrete prisms

Material	High performance concrete no silica fume (HPC/0SF)	High performance concrete 10% silica fume (HPC/10%SF)
Cement (kg)	430	431
Silica fume (kg)	n/a	45
Fly ash (type F) (kg)	74	87
Fine aggregate complying with CAN/CSA-A23.1 (kg)	653	602
Coarse aggregate complying with CAN/CSA-A23.1 (kg) Max. 10 × 5 mm	1083	1071
Water (L)	137	140
Air entraining agent complying with ASTM C 260 (darex)	As required	As required
Water reducer complying with ASTM C494, type A (WRDA 19) (L)	6.0	6.0
Superplasticizer complying with ASTM C 494, types B and D (Daratard 17) (L)	0.85	0.85
w/cm	0.27	0.25

TABLE II Physical properties of the cast concrete prisms [12]

Property	High performance concrete—no silica fume (HPC/0SF)	High performance concrete—10% silica fume (HPC/10%SF)
28 day compressive strength (MPa)	77.4	82.6
Resistivity (Ω · cm)	13000	52000

After the field exposure, channels, nominally 3 mm wide and 15 mm deep, were sawn into two of the four prisms of both mixes to position cracks subsequently induced under three-point bending using similar methods to that described in ASTM C 78-02. This test method was modified in that instead of flexural measurements, the induced crack of a particular prism was monitored using an optical micrometer until a surface displacement of approx. 0.3 mm was achieved. The overlapping positioning of the embedded five probe elements ensured that one of them was intersected by the induced crack. While under load, stainless steel wedges were used to maintain the induced crack opening and the corresponding static load. Channels were also sawn into the other two prisms of both concrete types but these prisms remained unloaded and uncracked to act as controls.

2.2. Exposure conditions & corrosion monitoring

Once the cracks had been formed and stabilized in the required prisms, all prisms were partially immersed in simulated sea water prepared in accordance with ASTM D1141 within large plastic containers such that the cracks were fully immersed. The sea water composition is given in Table III and was replaced every four months and continuously aerated.

Electrochemical measurements, open circuit potentials and linear polarization resistance, were performed at regular intervals for up to four years to assess the corrosion state of the prisms. Open circuit potential measurements were collected by measuring the potential difference between each of the embedded steel elements and a saturated calomel electrode (SCE) placed within the simulated sea water. Linear polarization resistance measurements, used as estimates of the corrosion rate for each steel element, were performed in accordance with the theoretical assumptions of Stern and Geary [11]: a saturated calomel reference electrode and 316 stainless steel counter electrode were electrically coupled to each steel element using an EG&G potentiometer that induced a potential difference ±20 mV around the open circuit potential of the steel, and measured the corresponding changes in electrical current. The initial results of these measurements, up to one year, have been reported in other work [12].

2.3. Materials characterization

2.3.1. Sectioning the prisms

The two prisms from both mixes of concrete that exhibited the highest corrosion rates were selected for further microstructural analysis. As anticipated, the prisms with the highest measured corrosion rates were the prisms with induced cracks. Two 50 mm diameter cores were taken from each prism, one of which included the crack and the rebar probe elements, as illustrated in Fig. 2, while the second was from an end of the prism, i.e., an unstressed area. The unstressed area cores were control samples for comparison with the cracked area cores. After coring, all exposed surfaces of the steel elements were immediately photographed to document the corrosion state of the steel and then promptly sealed in polyethylene bags.

TABLE III Chemical composition of simulated sea water (ASTM D1141). The pH (after adjustment with 0.1 N NaOH solution) was 8.2

Compound	Concentration (g/L)	Compound	Concentration (g/L)
NaCl	24.53	$NaHCO_3$	0.201
$MgCL_2$	5.2	KBr	0.101
Na_2SO_4	4.09	H_3BO_3	0.027
$CaCl_2$	1.16	$SrCl_2$	0.025
HCl	0.695	NaF	0.003

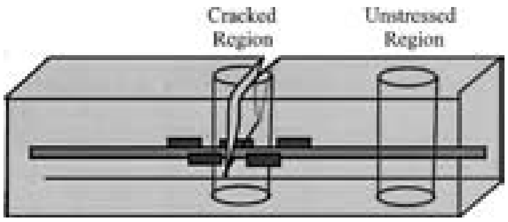

Figure 2 Location of cores taken for subsequent microstructural analysis.

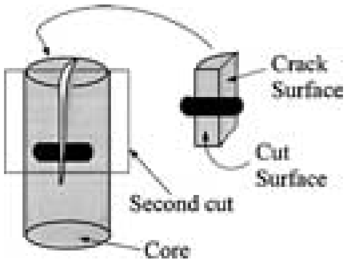

Figure 3 Sectioning the cores from the cracked region.

The cores taken from the ends of the prisms (i.e., unstressed areas) were sectioned lengthwise for chloride analyses and pore size distribution measurements described in Sections 2.3.2 and 2.3.3, respectively. Sectioning was performed either dry or using ISOPAR M (Exxon), a non-leaching synthetic isoparaffinic hydrocarbon. The cores from the cracked regions were also sectioned lengthwise, perpendicular to the induced crack, as detailed in Fig. 3, for the aforementioned chloride and pore size distribution measurements as well as additional microstructural analyses described in Section 2.3.4.

2.3.2. Chloride analyses

To measure the total chloride content (acid-soluble chlorides), which refers to both free chlorides and those chemically bound within the cement paste, ASTM C114, Section 19, was adapted for use with concrete samples to compensate for the presence of aggregate and this entailed testing a statistically meaningful quantity of material, approximately 10 g. The resulting chloride solutions were titrated against a silver nitrate solution using a Radiometer TIM800 semi-automatic titrator. This titrator slowly added a silver nitrate solution in increments as small as microlitres to determine the equivalence point of the chloride solution. The volume of titrant used to reach this point was used to calculate the chloride concentration for each solution. Every solution was analyzed three times to achieve an average value, and control solutions with a known chloride content were analyzed every three tests to estimate any external sources of chlorides such that they could be eliminated from the solutions under investigation.

2.3.3. Pore size distribution measurements
Representative concrete samples (approx. 10 × 10 × 10 mm each) were placed on a mesh stand in 200 mL of anhydrous isopropan-2-ol per sample to exchange the water in the samples with the solvent. The solvent was replaced daily for two days at which time the sample mass was constant within 0.1 mg. On the third day, the samples were placed in a vacuum dessicator for five days to evaporate the solvent.

A Micromeritics Poresizer 9310, capable of a maximum pressure of 200 MPa, was used for mercury intrusion porosimetry (MIP) measurements. Each sample was weighed, sealed inside a penetrometer, and then inserted into the Poresizer unit. After a vacuum of 0.4 kPa was achieved, the penetrometer was filled with mercury and the sample was incrementally pressurized to 200 MPa. The corrected pressure along with the volume of mercury intruded at each pressure change was used to calculate the pore size distribution. The resulting data was corrected for compression and thermal expansion of the mercury, and sample compression and volume changes of the glass penetrometer.

2.3.4. Microstructural analyses
Optical and environmental scanning electron microscopy sections were prepared with a Struers Discoplan TS (consisting of a precision saw and a planing cup blade) using ISOPAR M as a lubricant. Sections approximately 5–10 mm thick were produced with the precision saw. The sections were then mounted on glass slides and planed using a 35 μm cup blade. The flat specimens were then ground and diamond polished to a 1 μm finish using oil-based diamond suspensions and ISOPAR M to clean the surfaces between each polishing stage. Polished specimens were stored in a vacuum dessicator whose air had been evacuated and replaced with argon. Colour-indicating soda lime pellets and a reservoir of water were placed inside the dessicator to remove any carbon dioxide gas and humidify the chamber, respectively. The intent was to minimize the dessication, oxidation, or reduction of any of the corrosion products present.

Once the microscopy sections were prepared, the concrete adjacent to the induced crack, the surfaces of the crack, and their corresponding corrosion products on the surface of the steel were analyzed using environmental scanning electron microscopy (ESEM) with energy dispersive X-ray spectroscopy (EDS) as well as Raman spectroscopy. Samples of any corrosion products and the adjacent concrete were also analyzed with X-ray diffraction over the 2θ range of 5–70° using Cu K$_\alpha$ radiation.

The corresponding steel samples were subsequently pickled using an inhibited acid to remove the corrosion products without damaging the steel further. This solution, based upon antimony trioxide, stannous chloride, and hydrochloric acid, was prepared in accordance with ASTM G1, Solution C.3.1.

3. Results
3.1. Corrosion rate measurements
Fig. 4a shows the mean corrosion rates measured for the two prisms of both concrete types, both cracked and uncracked, for up to four years of exposure to the simulated sea water. The mean corrosion rates were calculated from the corrosion rates measured for the steel elements that were intersected by the induced crack or the centre element for the uncracked prisms. These data assumed that corrosion was taking place uniformly over the whole surface area of the probe elements. Initially, the steel in both concretes was corroding at higher than expected rates, which even surpassed that in similar industrial standard concrete prisms [12]. However, the rates for the HPC prisms gradually decreased with time to an order of magnitude lower than that in their industrial standard counterparts. The initially high rates for steel in HPC, both with and without silica fume, have been attributed to the higher density of microcracks with respect to normal quality concrete as well as

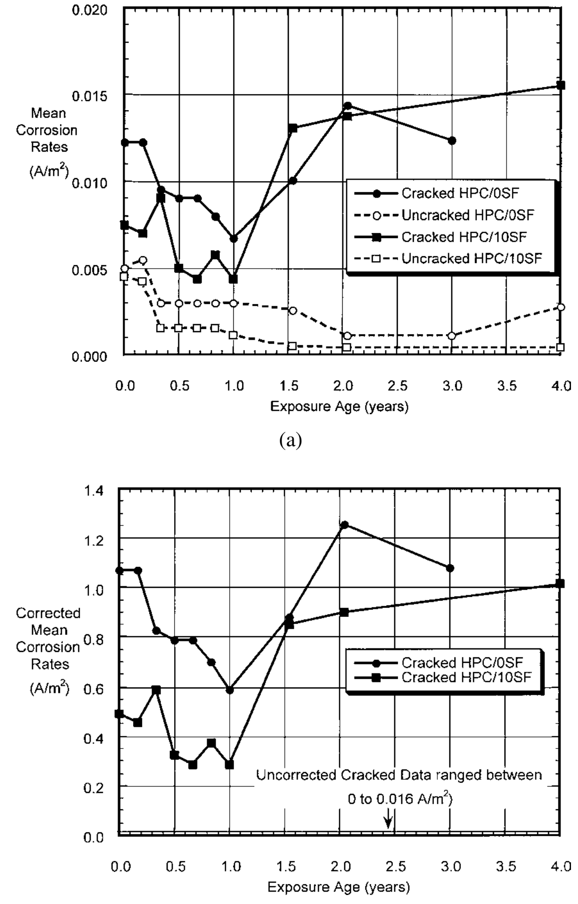

(a)

(b)

Figure 4 (a) Comparison of the mean corrosion current densities of the steel probes intersected by the crack in the cracked specimens and in the centre of the beams for the uncracked specimens. The corrosion current densities have been averaged over the entire probe surface area. (b) Comparison of the mean corrosion current densities of the steel probes intersected by the crack and corrected for the observed areas of active corrosion.

differences in the pore structure that would have affected the nature and extent of the capillary suction of moisture [12]. The subsequent decrease can be attributed to the ongoing hydration and pozzolanic reactions. These reactions would have been slower in the high performance concretes because of the limited water available for the reactions to proceed unless the concrete was cracked [13].

After about two years, the corrosion rate of the steel within the cracked HPC concretes began to increase while the steel within the uncracked concretes continued to decrease, indicating the obvious deleterious effect of cracking. It is important to note, however, that these corrosion rates for the cracked HPC concretes are low, i.e., they are similar to the corrosion rates measured for uncracked industrial standard concrete prisms [13], and are consistent with the reported observations of other researchers [7]. However, these corrosion rates increase almost two orders of magnitude once the data is corrected to account for the area of the steel that was actively corroding (described in Section 3.3). As such, these "local" corrosion rates can no longer be considered insignificant, as shown in Fig. 4b.

3.2. Macro- and microstructural observations of the concrete

3.2.1. Appearance and distribution of corrosion products

Immediately after coring, it was noted that only the cores taken from the induced crack regions of the prisms contained corrosion products and the distribution of the products changed if silica fume was present. As shown in Fig. 5, the corrosion products observed in the cracked region of the HPC/0SF did not accumulate preferentially at the steel/concrete interface but were distributed within the concrete cover up to 5 mm away from the steel/concrete interface. Moreover, two different corrosion products were identified, both by appearance and X-ray diffraction [13]: (a) akaganeite (β-FeOOH), which forms only in high chloride concentrations and in which some of the oxygen ions are replaced by chloride ions, was the yellow ochre product observed near the induced crack; and (b) goethite (α-FeOOH) was the dark brown corrosion product which formed farther away from the induced crack and was the more dense of the two products. ESEM micrographs of the goethite are presented in Fig. 6a and b and shows that some of the product was extremely dense and cracked with very few discernable features. EDS indicated that this product was predominantly iron but also contained calcium, silicon, and chlorine. A second layer of corrosion product consisted of a network of randomly-oriented hexagonal plates, approximately 5 μm across as shown in Fig. 6b. The crystalline plates contained relatively more calcium and chlorine. The presence of calcium and silicon in these products suggests that the corrosion products are intermingled with the cement constituents.

This intermingling was also observed with the akaganeite on a much larger scale. With the exception of some particles of relatively pure akaganeite shown in Fig. 7 (labelled "A"), most akaganeite was more easily identified by its composition than its morphology in high magnification micrographs. The akaganeite was intimately mixed with the cement paste to the extent that it was largely indistinguishable from the paste, as shown in Fig. 8. The presence of iron in the surrounding cementitious products suggests that iron species diffused to form preferentially within the void. The cracking of the matrix surrounding the iron-rich particle in Fig. 7 supports the theory that the expansion of corrosion products due to further oxidation and hydration causes internal tensile stresses within the concrete. It is thought that this particle once filled the void but that the low pressure of the ESEM removed some water from the product causing it to shrink. In the HPC/10%SF, corrosion product was observed only at the steel/concrete interface and within the induced crack, shown in Fig. 9 and labelled "C". This dense, dark brown/black product was identified as magnetite (Fe_3O_4) by Raman spectroscopy and a representative spectrum is presented in Fig. 10. Upon exposure to the ambient conditions of the laboratory for about 1 week, the magnetite at the steel/concrete interface oxidized to haematite (α-Fe_2O_3) and goethite (α-FeOOH) which underlines

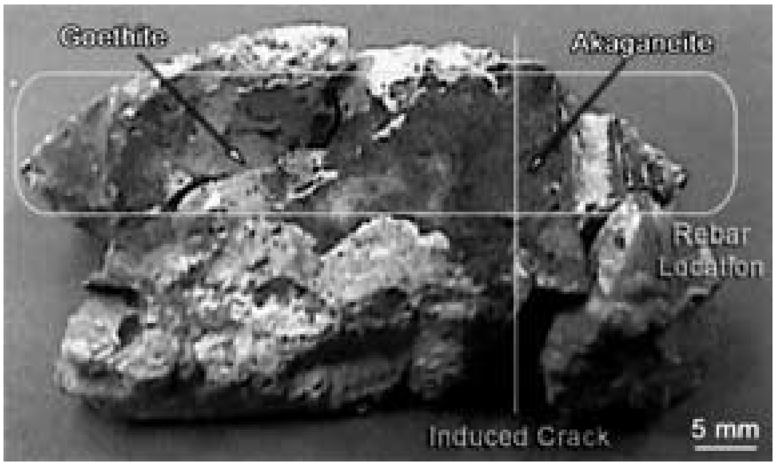

Figure 5 Fractured section of the HPC adjacent to the rebar showing two types of corrosion product, one dark brown (goethite, α-FeOOH) and the other, a "dirty" yellow ochre colour (akageneite, β-FeOOH) within which some of the oxygen ions are replaced by chloride [4].

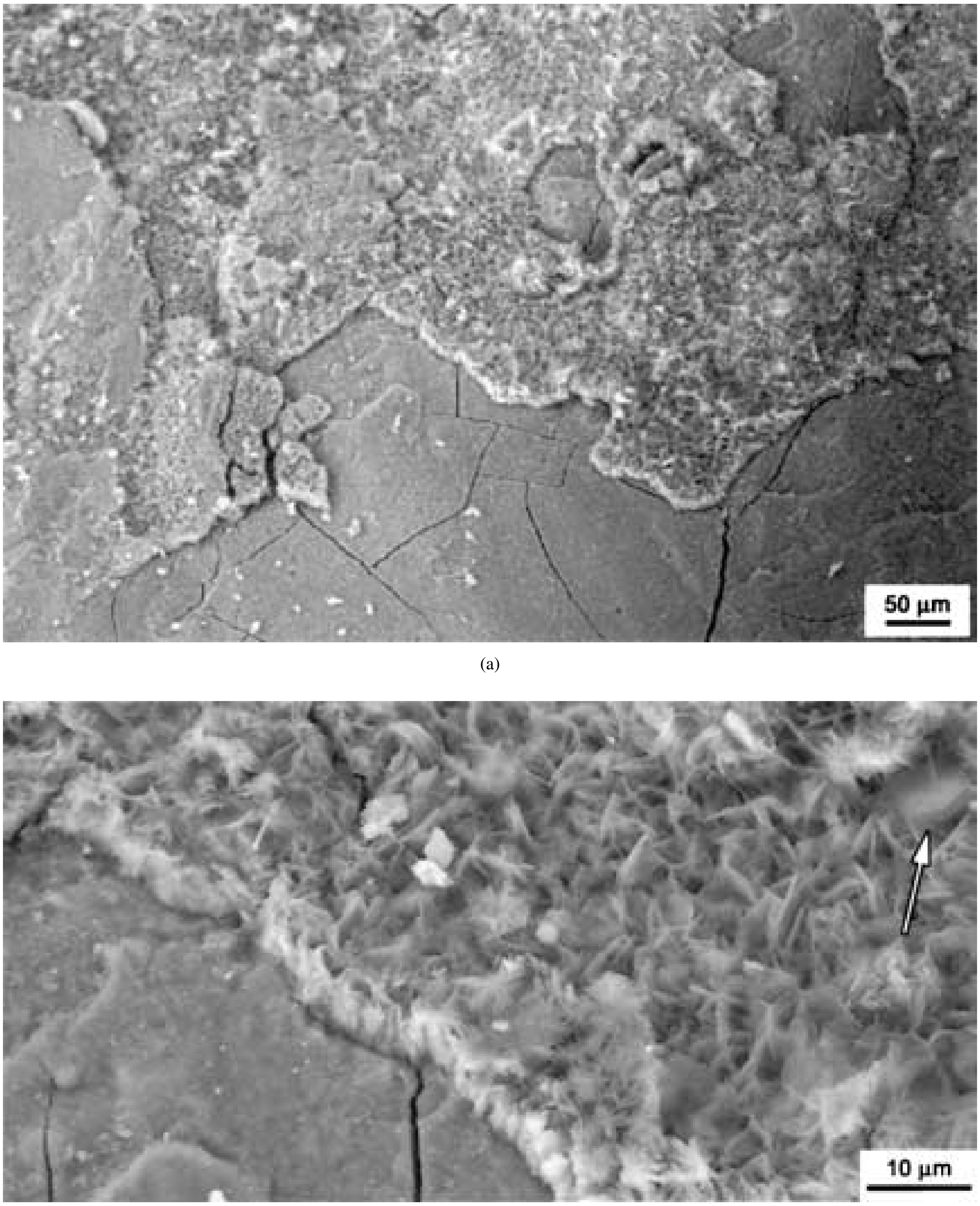

(a)

(b)

Figure 6 (a) Micrograph of goethite (α-FeOOH) observed at steel/concrete interface in high performance concrete without silica fume, HPC/0SF [4]. (b) Magnification of the central region of Fig. 6a showing two layers of corrosion product: the "bottom" dense, featureless layer except for the cracks, and the "top", distinctly crystalline layer. Note the clearly hexagonal crystal in the upper right corner.

the importance of *in situ* rather than *ex situ* observation of corrosion products. The magnetite within the induced crack remained relatively unaffected because of the limited surface area of the product within the crack. High magnification elemental maps of a representative area of the induced crack, presented in Fig. 11, shows that the internal width of the crack was approximately 200 μm and was densely and completely filled with magnetite as evidenced by the iron elemental map. In addition, the surfaces of the crack were lined with a magnesium product, presumably from the formation of brucite ($Mg(OH)_2$) upon exposure to the simulated sea water and prior to the deposition of the corrosion products. No other corrosion products were observed in this material.

3.2.2. Chloride measurements

Chloride content measurements are presented in Table IV and show that, as anticipated, if HPC concretes remain unstressed and uncracked, chloride diffusion is so slow that chlorides cannot be detected within 10 mm

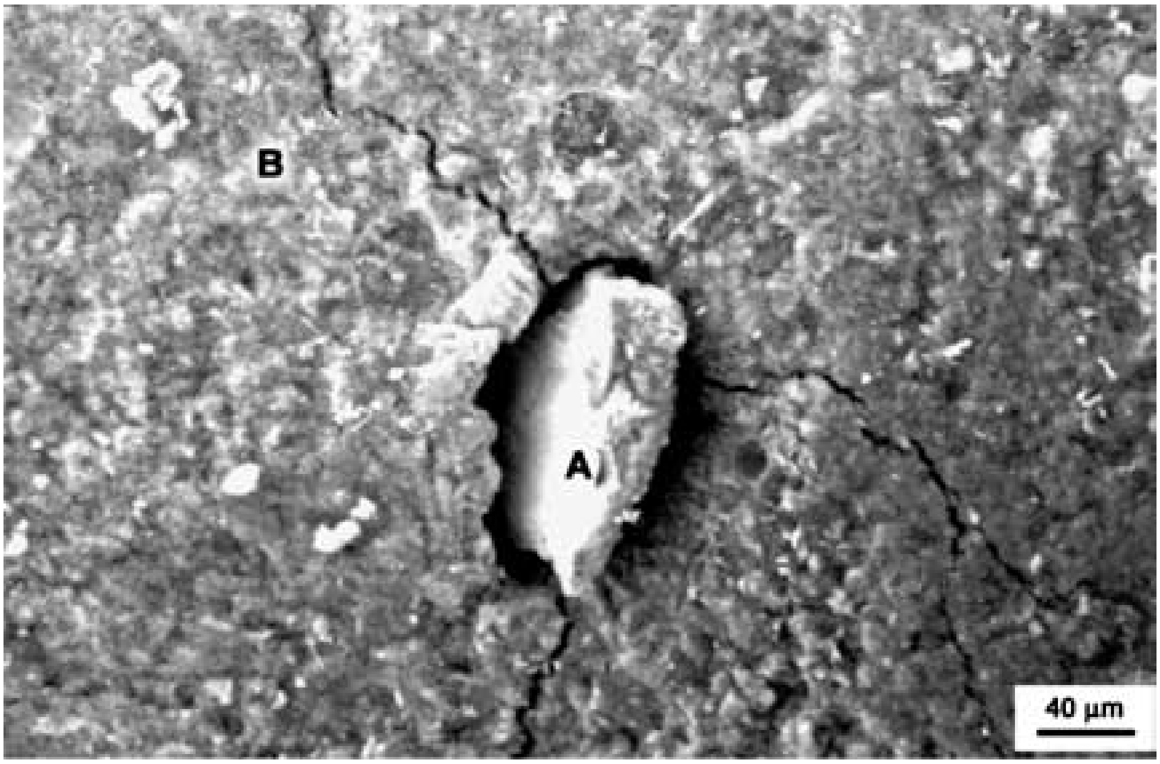

Figure 7 Akaganeite (β-FeOOH) in high performance concrete without silica fume. Regions of corrosion product containing approximately 40 at% Fe are labelled "A" while the surrounding material containing approximately 18 at% Fe is labelled "B" [4].

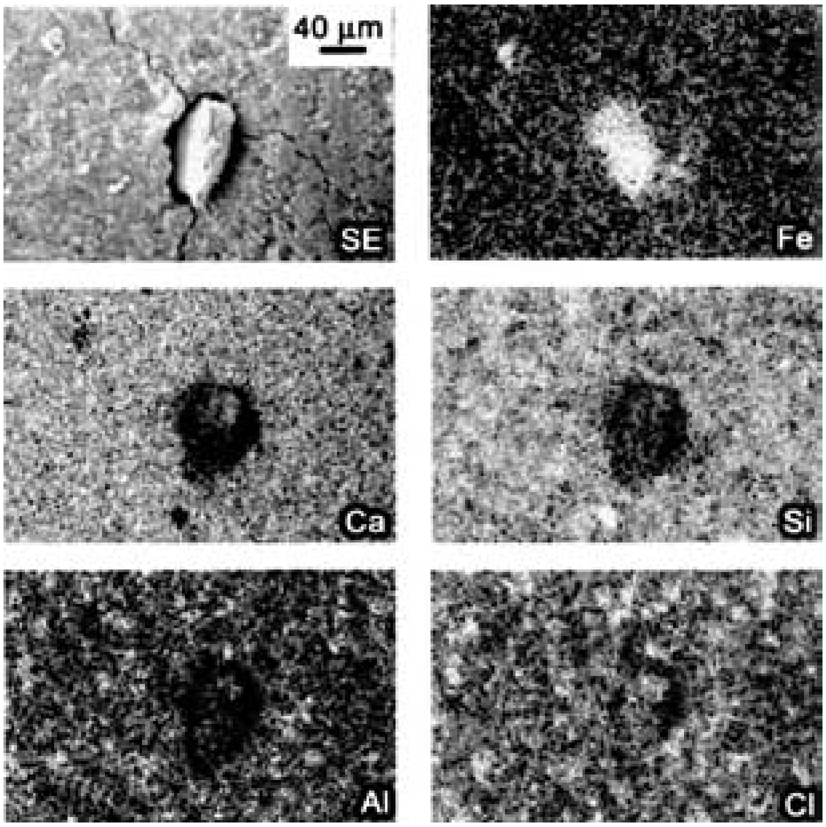

Figure 8 Elemental maps of the embedded corrosion product shown in Fig. 7 [4].

of the surface of the steel after at least three years exposure to simulated sea water (detection limit of the technique of about 1 ppm by mass). The concrete cover depth in this region was nominally 40 mm which is approximately the minimum allowable cover depth in reinforced concrete structures for this exposure class (CAN/CSA A23.1-M90, Section 15.1.7.1).

Significant chloride levels were detected near the induced crack of the prisms in the same period of time, however, which demonstrates that cracks are

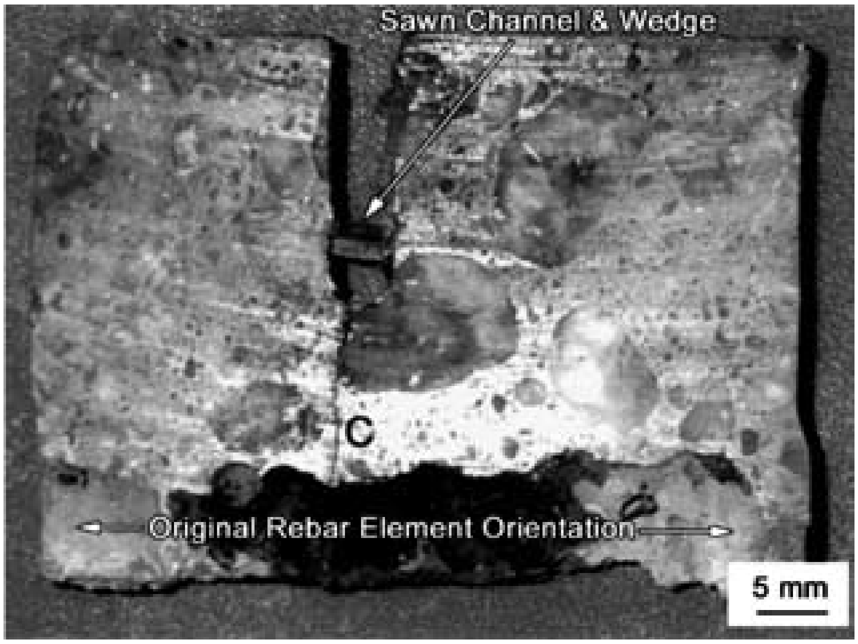

Figure 9 Macrophotograph of HPC/10%SF core section showing the induced crack that is plugged with magnetite [4]. The induced crack is to the left of the label "C".

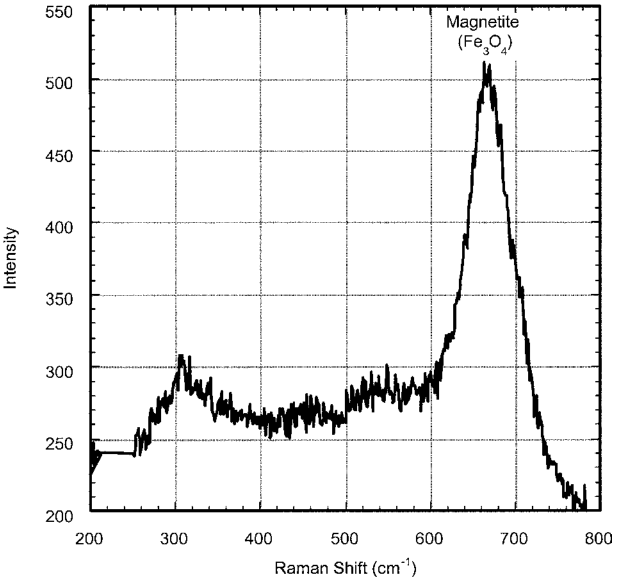

Figure 10 Raman spectrum of the dense, dark brown-black corrosion product, magnetite (Fe_3O_4), observed at the steel/concrete interface of both HPCs which also filled the induced crack of the HPC/10%SF.

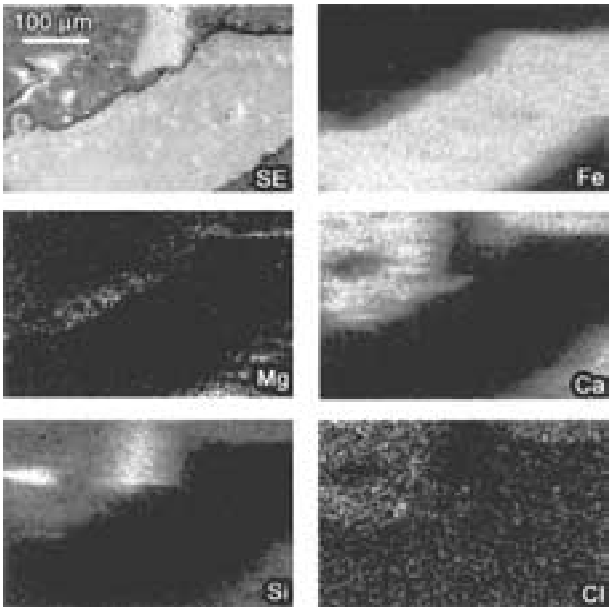

Figure 11 Elemental maps of the induced crack region of HPC/10%SF noted in Fig. 9.

a significant issue to be addressed for the long-term service life of reinforced concrete structures: the chloride content near the induced cracks in the HPC/0SF was approximately 3.42 mass% cement while the corresponding value for HPC/10%SF was 0.21 mass% cement. Current American Concrete Institute standards (Committee 222-Corrosion of Metals) suggest a maximum acid soluble content of 0.2% by mass cement based upon field studies of bridge decks. The values presented in Table IV are estimates of the total chloride content (i.e., acid-soluble chlorides) and are, therefore, intended to present the worst-case scenario for chloride exposure.

Under these circumstances, the resulting chloride content near the induced crack of both concrete types exceeded the recommended limit for corrosion. Overall, the HPC/10%SF had a chloride content that was at least an order of magnitude lower than its counterpart without silica fume, and barely exceeded the water-soluble and acid-soluble chloride limits even after four years exposure to the simulated sea water. To properly interpret these levels, however, it must be noted that the HPC/0SF was sectioned after three years exposure to the simulated sea water while the HPC/10%SF was sectioned after four years. It is, therefore, possible that the HPC might have had an even higher chloride level if it were exposed to the simulated sea water for an additional year.

These chloride levels can be explained by the different pore structures for both concretes that resulted

TABLE IV Mean acid-soluble chloride contents of concrete within 10 mm of the steel/concrete interface from the regions indicated in Fig. 2. Values are the mean of triplicate samples from two prisms

Concrete type	Exposure age (years)	Chloride content at crack (mass% concrete)	Chloride content at crack (mass% cement)	Chloride content in unstressed region (mass% concrete)
HPC/0SF	3	0.726 ± 0.0003	3.42 ± 0.0014	Not detected
HPC/10%SF	4	0.050 ± 0.0001	0.21 ± 0.0004	Not detected

from the presence of silica fume. The reaction products of silica fume have been shown to block capillary pores [2] and could ameliorate any microcracks which would enhance the connectivity of the pore network. The HPC/10%SF had a similar low w/cm ratio as its counterpart, HPC/0SF, but the presence of silica fume reaction products made the network of fine capillary pores more discontinuous and blocked any microcracks. Thus, the benefit of a low w/cm ratio to reduce the ingress of chlorides can only be realized with the addition of silica fume or any other admixture that would make the pore network more discontinuous.

3.2.3. Pore size distribution measurements

Fig. 12 shows a comparison between the pore size distributions of the HPC/0SF for concrete samples near the induced crack and those in the corresponding unstressed region. The profiles are similar with threshold pore diameters of about 0.03 μm for both regions, indicating that there was no statistical difference between the two types of samples. In contrast to the results of the HPC/0SF samples, Fig. 13a and b show the variable profiles of six replicate samples for the unstressed and induced crack regions of the HPC/10%SF prisms, respectively. In the unstressed region, the pore size distributions for the HPC/10%SF were similar to the HPC/0SF distributions with the exception of some microcracks approximately 8–10 μm in size in three of the samples, and a slightly smaller pore threshold diameter of 0.02 μm. The presence of these microcracks in the HPC/10%SF is consistent with the observations and conclusions of Sellevold *et al.* [2] who reported that the relatively rapid pozzolanic reactions of the silica fume refines or disrupts the capillary pore network, effectively sealing the pore network of the concrete. This reduces the access of water into the concrete and the corresponding self-dessication results in the observed microcracking. Near the induced crack, the 0.02 μm pore threshold diameter was maintained, but the microcracks were observed in only one of the six samples and pores in the 0.01–10 μm range were not detected. From these samples, it is clear that the induced crack exposed the self-dessicated HPC/10%SF to sea water which rehydrated this internal region of the concrete, and allowed further pozzolanic and hydration reactions to occur. This suggests that the inevitable cracking that occurs in reinforced concrete structures may be beneficial for silica fume HPC with respect to a reduction in the overall steel chloride exposure.

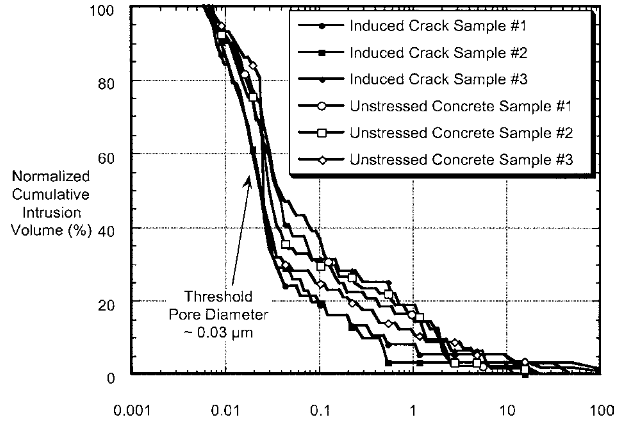

Figure 12 Comparison of the pore size distributions for concrete samples from the unstressed and induced crack regions of the HPC/0SF prisms.

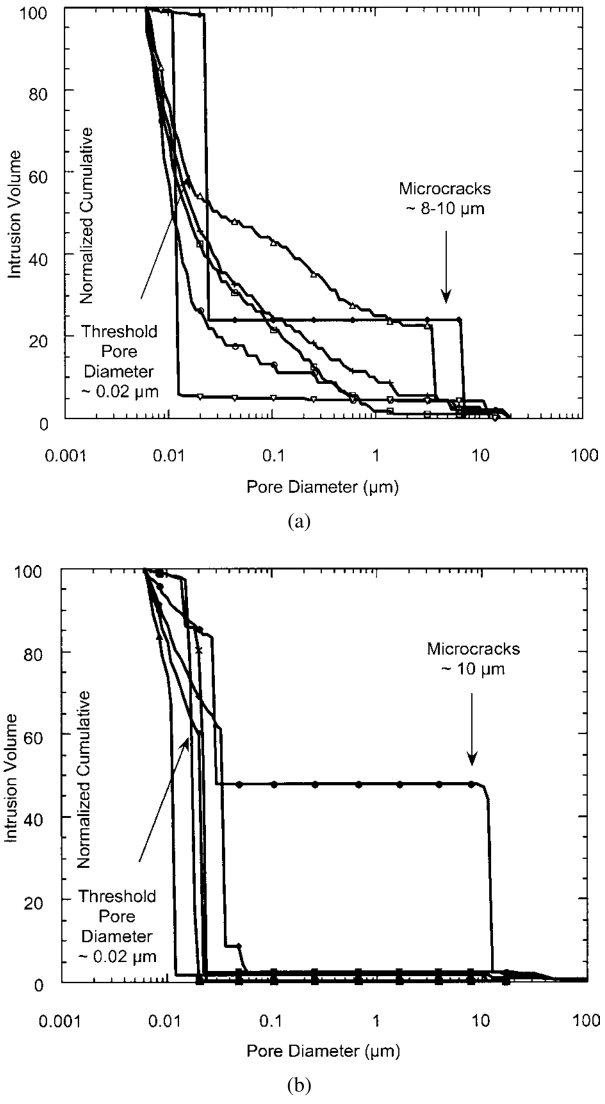

Figure 13 (a) Pore size distributions of six replicate concrete samples from the unstressed region of the HPC/10%SF prisms. (b) Pore size distributions of six replicate concrete samples from the induced crack region of the HPC/10%SF prisms.

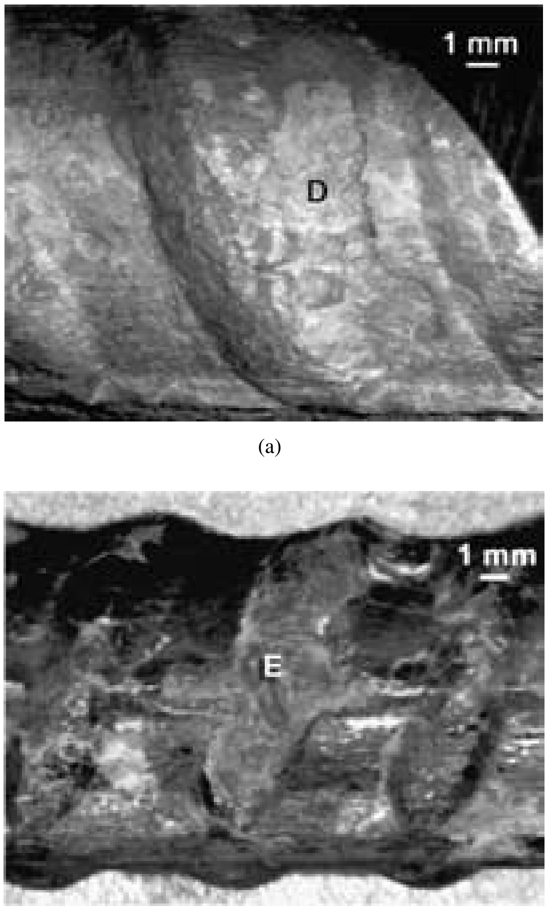

Figure 14 (a) Macrophotograph of the steel surface adjacent to the induced crack region of the HPC/0SF. The area of deeper macro-corrosion damage is labelled “D”. (b) Macrophotograph of the steel surface adjacent to the induced crack region of the HPC/10%SF. The area of deeper macro-corrosion damage is labelled “E”.

3.3. Corrosion products on the surface of the steel

As noted in Section 3.2.1, no corrosion products were observed on or near the steel in the unstressed, uncracked ends of the prisms. However, the steel retrieved from the HPC/0SF showed a relatively uniform distribution of corrosion products while the steel retrieved from the HPC/10%SF showed an accumulation of corrosion product only where the crack intersected the steel. When these corrosion products were removed and the surfaces observed with a stereomicrosope capable of scaled measurements, the steel retrieved from the HPC/0SF contained fairly large superficial pits, more wide (of the order of several millimetres) than deep, as shown in Fig. 14a and labelled “D”. The corrosion was located predominantly in the region between the ribs with about 20% of the total surface of the steel active. In contrast, the steel retrieved from the HPC/10%SF had only one region of damage, indicated as “E” in Fig. 14b. This region represented only about 5% of the total surface of the steel but the corrosion was much deeper and appeared as if the corrosion process were cutting this steel like a knife.

TABLE V Comparison of corrosion damage to steel probe elements

Concrete type	Approximate macro-corrosion pit dimensions	Approximate macro-corrosion pit depth (mm)	Estimate of lost steel cross-sectional area
HPC/0SF	3 × 9 mm	0.9	8%
HPC/10%SF	3 × 12 mm	2.0	14%

Note: Does not include those pits unresolvable with the unaided eye.

These macrocorrosion pit geometries are summarized in Table V along with an estimate of the cross-sectional area of the steel that has been destroyed by the corrosion process. Thus, the steel retrieved from the HPC/10%SF suffered greater damage than the steel in the HPC/0SF and this indicates that a high concrete electrical resistivity can have negative consequences. Using the approximate pit dimensions from Table V, the previously calculated mean corrosion rates of steel in cracked prisms (Fig. 4a) was corrected for the macroscopic area of the steel actually corroding, as shown in Fig. 4b. Once these corrections have been performed, their rates increased by two orders of magnitude. Presumably, higher electrical resistivities do not allow large separation of cathodes and anodes on the surface of the steel, thereby localizing any macrocell corrosion attack and emphasizing the role of microcell corrosion (where the anodic and cathodic half-cell reactions take place at essentially the same location). In effect, steel in cracked concrete with a high electrical resistivity can potentially suffer corrosion with consequences as severe as that in concrete with a low resistivity. Under these circumstances, the type and distribution of the corrosion products and whether they fill the cracks, in combination with the tensile strength of the concrete, would govern the long-term durability of the concrete. This type of observation also underscores the difficulty in making valid corrosion rate measurements when the area of the corroding region cannot be known or even estimated non-destructively. In consideration of these factors, it then becomes clear why the propagation phase of service life models has not been as well developed as the initiation stage of corrosion.

4. Discussion

It is clear that the effect of silica fume on the corrosion resistance of steel in high performance concrete is complex. The reaction of silica fume had the anticipated effect on the electrical and microstructural characteristics of high performance concrete: its high electrical resistivity (Table II) corresponded to the decrease in the size and the number of continuous pores, shown by Fig. 13b. This had a strong impact on the ability of chlorides to ingress into the concrete: the HPC/10%SF near the induced crack had a chloride concentration only about 7% of that in a similar region of the HPC/0SF fume even after an extra year of exposure to the simulated sea water. These observations are consistent with the reported experiences of other researchers [7].

In spite of these enhanced properties, corrosion did initiate in the cracked region of both concretes within the period of study, up to four years. Although the chloride content was very low in the 10 mm layer of concrete adjacent to the steel/concrete interface, those that were present were concentrated very close to the surface of the induced crack (Fig. 11) and where the crack tip intersected the steel, consistent with the observations of Rodriguez and Hooton for conventional concrete mixes [8]. Contributing to the corrosion attack was likely a decrease in the chloride threshold value resulting from the reaction of the silica fume lowering of the pore solution pH, a widely reported phenomenon.

As such, the resulting corrosion products that formed in the HPC/10%SF were entirely different from the products that formed in the HPC/0SF. In addition, the former were confined to the space provided by the induced crack and the steel/concrete interface, while corrosion products in the HPC/0SF were more uniformly spread throughout the concrete cover and not confined to either the steel/concrete interface or the main crack. Moreover, the corrosion products that formed within the HPC/0SF cover some distance from the rebar appeared to have cracked the concrete, as shown in Fig. 7. This indicates that the pozzolanic reaction of the silica fume had two main effects: (a) it sufficiently densified and strengthened the concrete such that damage was reduced; and (b) the reaction occurred before any corrosion products could diffuse into the concrete cover, and any that were present were confined to the induced crack (i.e., the observed magnetite (Fe_3O_4)). The latter effect suggests the benefit that any corrosion products that form in the silica fume concrete would plug the crack, effectively barring further direct chloride and oxygen exposure to the surface of the steel. The fact that magnetite formed (i.e., a corrosion product which forms in oxygen deprived conditions) supports this conclusion. Thus, the pozzolanic reaction of silica fume densified the concrete and reduced the exposure of the steel to chlorides and oxygen by the formation of corrosion products which resulted in the low average corrosion rates that were observed over a four year period during this research programme and others [7].

This may have a potential drawback, however. The more uniform, superficial damage to the steel within the HPC/0SF shown in Fig. 14a may be preferable to the localized damage resulting from the presence of silica fume in the HPC/10% SF shown in Fig. 14b. It is possible, however, that the damage observed on the surface of the steel was the most that was to occur and that if the prisms had remained uncored, the corrosion rate may have decreased even further over time due to the plugged crack and the restrictions to oxygen and water diffusion it would have imposed provided that the tensile strength of the HPC could accommodate the additional tensile stresses.

Overall, there are two important observations of this work which should be taken into account in service life prediction. The first is that the corrosion products formed had specific volumes of between 2.1 and 3.5 (reported values as pure minerals) rather than 6+ normally assumed to be responsible for the cracking. This volume expansion was large enough to crack the HPC/0SF but not the HPC/10%SF because of the aforementioned effects on the cement paste by the silica fume. It is possible that further oxidation or wet/dry cycling could increase these volumes but further experimentation is required to confirm this hypothesis. The second observation is that significant local variations in the chemistry of the concrete can occur during corrosion as indicated by the formation of akaganeite only near the main crack in the HPC/0SF, a product which normally forms only in high chloride concentrations and at lower pH values. The effect of varying product composition on crack formation is also a factor that requires further investigation.

5. Conclusions

In general, the observed behaviour of these high strength (>70 MPA), high performance concretes is not as anticipated. Premature of corrosion of steel in both high performance concretes was observed—albeit at low rates. These rates initially appeared to be less significant with time as they decreased to under 0.016 A/m^2. However, once these rates were corrected for the area of steel actually corroding, the corrosion rates were almost two orders of magnitude higher and no longer insignificant in highly localized areas. Thus, corrosion occurring in cracked high performance concretes is potentially more insidious and destructive because corrosion rates will be underestimated by non-destructive techniques such as LPR. This issue was more pronounced for the steel in the cracked high performance concrete containing silica fume, and can be attributed to its inherently high electrical resistivity that decreases the permitted distance between cathodes and anodes on the surface of the steel.

On the other hand, the presence of silica fume was observed to limit the composition and formation of corrosion products: magnetite (Fe_3O_4), an oxygen-limited product, was observed only within the space of the induced crack and corrosion products were not observed elsewhere in the concrete cover. A similar effect was noted in the measured chloride levels as the HPC/10%SF contained approx. 7% of the chlorides measured in the HPC/0SF (0.21 vs. 3.42 mass% cement). As such, the addition of silica fume to high performance concrete mixes can be considered beneficial.

Overall, it is well-understood that uncracked, impermeable concrete provides the best protection for steel in a chloride-environment. Should, however, this impermeable concrete become cracked because of structural overloading or shrinkage, extra precautions must be taken to prevent the more localized and insidious corrosion damage (i.e., corrosion accompanied by little or no rust staining in the cover that would signal a problem) from accumulating at the steel/concrete interface until a catastrophic failure occurs. It is, therefore, recommended that particular attention be paid to cracks in high performance concrete structures such that this issue can be addressed in an economically efficient manner, and ensure that the anticipated service life of these structures is achieved.

Acknowledgements

The financial support of the Natural Sciences and Engineering Research Council of Canada through Concrete Canada and a Collaborative Project grant is gratefully acknowledged. We are thankful for the design and construction of the concrete prisms by Delta Catalytic Inc., the collaboration of Mr. P. T. Seabrook of Levelton Engineering Inc., and Mr. Robert Weiermair for the initial mechanical and electrochemical measurements. The assistance of Mr. Marek Odziemkowski with the Raman spectroscopy technique was also greatly appreciated.

References

1. CONCRETE CANADA, Networks of Centres of Excellence Annual Report, Meeting the Challenges of the Third Millenium—High Performance Concrete Structures (1997).
2. E. J. SELLEVOLD, D. H. BAGER, E. KLITGAARD and T. KNUDSEN, Report BML 82.610, 1982, Division of Building Materials, Norwegian Institute of Technology, NTH, Trondheim, Norway, p. 19.
3. R. JOHN and S. P. SHAH, *J. Mater. Civil Eng.* **1** (1989) 185.
4. D. DARWIN, S. BARHAM, R. KOZUL and S. LUAN, *ACI Mater. J.* **98** (2001) 410.
5. A. DELAGRAVE, J. MARCHAND, *et al.*, Durability of High Performance Cement Pastes in Contact with Chloride Solutions, in Proceedings of the Fourth International Symposium on the Utilization of High Strength/High Performance Concrete, edited by F. de Larrard and R. Lacroix, Paris, France, 1996, p. 479.
6. M. T. LIANG, K. L. WANG *et al.*, *Cem. Concr. Res.* **29** (1999) 1411.
7. K. PETTERSSON and P. SANDBERG, Chloride Threshold Levels, Corrosion Rates and Service Life for Cracked High-Performance Concrete, in Proceedings of the Fourth CANMET/ACI International Conference on the Durability of Concrete (SP-170), Sydney, Australia, 1997, p. 451.
8. O. G. RODRIGUEZ and R. D. HOOTON, *ACI Mater. J.* **100** (2003) 120.
9. J. PAULSSON-TRALLA and J. SILFWERBRAND, *ACI Mater. J.* **99** (2002) 27.
10. P. GOLTERMANN, *ibid.* **100** (2003) 114.
11. M. STERN and A. L. GEARY, *J. Electrochem. Soc.* **104** (1957) 56.
12. R. WEIERMAIR, C. M. HANSSON and P. T. SEABROOK, Electrochemical Noise Measurements of Cracked High Performance Concrete Exposed to Marine Environments, in Proceedings of the Third CANMET/ACI International Conference on the Performance of Concrete in Marine Environments, Supplementary Volume, St. Andrews-by-The-Sea, N.B., Canada, 1996, p. 203.
13. T. D. MARCOTTE and C. M. HANSSON, A Comparison of the Chloride-Induced Corrosion Products from Steel-Reinforced Industrial Standard Versus High Performance Concrete Exposed to Simulated Sea Water, in Proceedings of the Conference on High Performance and Reactive Powder Concretes, Sherbrooke, P.Q. Canada, August 1998, edited by P. C. Aïtcin and Y. Delagrave (Concrete Canada, 1998) Vol. 4, p. 145.

Received 9 April 2002
and accepted 7 July 2003